Materials Characterization 122 (2016) 54–62

Contents lists available at ScienceDirect

Materials Characterization

journal homepage: www.elsevier.com/locate/matchar

As cast precipitation microstructures in twin-roller melt-spun $Cu_{90}Co_{10}$ alloys

H. Núñez-Coavas [a], G. Pozo-López [a,b,c,*], A.M. Condó [b,d], S.E. Urreta [a], L.M. Fabietti [a,b,c]

[a] Facultad de Matemática, Astronomía y Física, Universidad Nacional de Córdoba, Ciudad Universitaria, 5000 Córdoba, Argentina
[b] Consejo Nacional de Investigaciones Científicas y Técnicas (CONICET), Argentina
[c] Instituto de Física Enrique Gaviola – CONICET, Argentina
[d] Centro Atómico Bariloche, Comisión Nacional de Energía Atómica, Instituto Balseiro, Universidad Nacional de Cuyo, Av. Bustillo 9500, 8400 San Carlos de Bariloche, Argentina

ARTICLE INFO

Article history:
Received 5 August 2016
Received in revised form 5 October 2016
Accepted 6 October 2016
Available online 7 October 2016

PACS:
75. Fabrication of magnetic nanostructures;
75.75.-c Magnetic properties of nanostructures

PACS:
75. Fabrication of magnetic nanostructures
75.75.-c Magnetic properties of nanostructures
Keywords:
Twin-roller melt spun CuCo
Granular magnetoresistance
Interacting superparamagnets
Dipolar interactions

ABSTRACT

As cast $Cu_{90}Co_{10}$ ribbons rapidly solidified by twin-roller melt spinning, exhibit special microstructure features. This processing method provides scenarios where a different phase selection takes place; coherent Co precipitates form directly from solidification, with neither a spinodal-like composition oscillation nor a discontinuously precipitated laminar phase. Samples are processed at tangential wheel speeds of 10 m/s (V10), 15 m/s (V15), 20 m/s (V20) and 30 m/s (V30). Microstructures resulting from this single step process are characterized and the hysteresis properties and the magnetoresistance effects evaluated. Samples V30 have a quite uniform density of coherent precipitates, with a narrow size distribution around 4 nm. On contrary, non-uniform precipitate distributions are found in samples cooled at lower rates; zones with a high density of coherent Co-rich precipitates are found forming colonies. These colonies are consistent with the extended compositional fluctuations occurring during very early stages in the cooling process. Samples may exhibit wide (V10) and even bimodal (V15) size distributions. Only samples V30 behave close to the ideal superparamagnetism. Samples V20 present relatively large coercivity and relative remanence and behave as an interacting superparamagnet, while the hysteresis loops of ribbons cooled at lower rates exhibit a ferromagnetic contribution in addition to the superparamagnetic-like one. This ferromagnetic component arises from blocked precipitates, larger than the upper bound size for superparamagnetic behavior at 300 K (12 nm). Room temperature magnetoresistance values associated to granular scattering units decrease as the mean precipitate size increases, but they remain below 2%, which is lower than that measured in samples annealed after rapid solidification, indicating that in this latter case contributions from the spinodally segregated matrix take place in addition to that of Co granules.

1. Introduction

The Cu–Co [1] system presents a high positive heat of mixing as well as a wide metastable region. Due to its versatile and interesting properties it has been matter of extensive research. As the constituent elements are immiscible in a large composition range, the system is considered a model to investigate decomposition and precipitation processes. Depending on the alloy composition and the thermo-mechanical production route, rapid solidification and further annealing may promote coherent precipitate distributions [2], spinodal decomposition solute profiles [3], and/or discontinuous precipitation of a lamellar phase [4].

In low Co systems (5–15 at.% Co), small Co-rich precipitates may be introduced into the Cu matrix by heat treatments, usually leading to an ideal superparamagnetic behavior. In this composition range spin glass behavior has also been reported at low temperature [5].

In addition, depending on composition and thermal treatment, these binary alloys exhibit spin dependent electron transport, evidenced by Kondo-like scattering [6] and giant magnetoresistance (GMR) effects [7].

Different authors have observed GMR in $Cu_{90}Co_{10}$ ribbons solidified at high rates by melt-spinning and further treated for 1 h at 723 K [7], or Joule heated during different periods of time [8]. The effect was first attributed to electron scattering by the coherent Co-rich precipitates formed during annealing, after the casting step. Models [9,10] developed to describe this *granular* magnetoresistance (MR) assume that Co precipitates are independent superparamagnetic units, embedded in a high conductivity, diamagnetic Cu matrix. However, hysteresis loops corresponding to the microstructure leading to optimum MR exhibit small and symmetric coercivity, which has been attributed to dipolar interaction between Co-rich coherent precipitates (*interacting superparamagnetism*) and/or to the Co-rich 'lames' in the spinodally separated matrix [11–13].

* Corresponding author at: Facultad de Matemática, Astronomía y Física, Universidad Nacional de Córdoba, Ciudad Universitaria, 5000 Córdoba, Argentina.
E-mail address: gpozo@famaf.unc.edu.ar (G. Pozo-López).

http://dx.doi.org/10.1016/j.matchar.2016.10.007
1044-5803/

More recently, GMR phenomenon has been attributed to both, the discontinuous precipitation of the lamellar phase [14], and the development of large amplitude composition modulations, associated with spinodal decomposition [15,16]. In these cases, *multilayer-like* electronic scattering effects are proposed instead of granular ones. In this scenario, Co-rich regions are likely to contribute to full magnetization with a ferromagnetic component, leading to the observed hysteresis.

In previous articles [6,17] we have reported that twin-roller melt-spinning techniques are suitable to obtain the desired precipitation substructure directly from the melt, in a single step, just by selecting the adequate casting conditions. In the reported results, casting conditions led to a microstructure in which Co coherent precipitates coexist with segregation strips of about 50 nm wave length, exhibiting MR behavior up to 0.8% at 300 K and 0.85 T. This modulation was attributed to spinodal decomposition, despite the predicted XRD configuration for this case (a central peak and two satellite peaks corresponding to the different compositions) is not observed. In fact, pure Cu (111) peak splits only in two, which is more consistent with the presence of the lamellar phase reported in [4,14].

Twin-roller melt-spinning [18–20] is a rapid solidification route imposing cooling rates between 10^5 and 10^6 K/s which may be combined with a hot rolling process. It is a semi-solid metal molding technology successfully applied to metallic ribbons production; twin-roll casting directly produces a ribbon by pouring molten metal into a pair of rotating copper wheels. The liquid metal flows through a nozzle into a molten bath built between the twin-rolls in the stationary regime. Solidification occurs while the liquid metal flows from the entrance to the export section, transferring most of the heat energy to the water-cooled twin rolls. Depending on the applied conditions, plastic deformation may occur (hot rolling).

During twin-roller melt-spinning, solidification commences by nucleation at the roll surface and rapidly expands by dendritic growth as the molten metal exits the feeding nozzle. During the initial stage, the solidified metal is in contact with the roll so the heat is transferred by conduction. Then, the rotating rolls reduce the metal to the final gauge.

As solidification progresses, different scenarios may be identified: either the solidified metal grows columnar-like, normally up to the ribbon plane and is reduced to the final gauge by the rotating rolls; or the symmetric heat extracting gradients become relatively small, promoting nucleation in the remaining liquid in the central part of the ribbon, leading to equiaxed grains; or, a combination of these two leading to both equiaxed and columnar grain structures.

The microstructure of $Cu_{90}Co_{10}$ alloys processed by twin-roller melt-spinning is thoroughly characterized, for the first time, in this work. In addition, the correlations between the precipitation substructure and both, the observed hysteresis and magnetoresistance properties, are investigated assuming interacting superparamagnetism models [11–13,21], and also considering large magnetically blocked precipitates.

Size and spatial distributions and volume density of coherent Co precipitates are correlated with the observed deviations from the ideal superparamagnetic behavior.

2. Experimental Procedures

A master alloy of nominal composition $Cu_{90}Co_{10}$ was prepared by arc melting 99.99% Cu (Alfa Aesar) and 99.95% Co (Alfa Aesar). The small ingots obtained (about 5 g) were further re-melted four times to promote a homogeneous distribution of the components. All procedures were conducted under a Zr gettered Ar atmosphere. The weight loss in the different ingots during arc melting was <0.2%. Then, the alloy was processed in a twin-roller melt- spinning device at four different tangential wheel speeds: 10 m/s, 15 m/s, 20 m/s and 30 m/s to obtain samples V10, V15, V20 and V30, respectively. The springs forcing the contact between the two rolling wheels were set to 24 N. Ribbons of about 1.3–1.7 mm wide and 50–90 μm thick were obtained. No differences among the ribbons faces could be observed, indicating good contact and symmetric solidification conditions.

The resulting microstructures were characterized by X-ray diffraction (XRD), scanning electron microscopy (SEM) and transmission electron microscopy (TEM). X-ray diffraction profiles were recorded in a Philips PW 3020 diffractometer in the 2θ range from 20° to 100°, in Bragg-Brentano configuration, using CuKα radiation ($\lambda = 1.5418$ Å) and a graphite monochromator. Samples observed by TEM were thin foils prepared by twin-jet electropolishing in a 500 ml distilled water, 250 ml ethanol, 250 ml H_3PO_4 (orthophosphoric acid), 50 ml C_3H_8O (1-propyl alcohol) and 5 g of urea electrolyte, at 276 K and 12 V. Transmission electron microscopy observations and selected area diffraction patterns were performed in a Philips CM 200 UT microscope, operating at 200 kV and equipped with energy-dispersive X-ray spectroscopy (EDS) facility.

Magnetic measurements were performed in 4 mm long as-cast ribbons with the applied field parallel to the sample length, so the demagnetizing factors N_z [22] resulted 0.016 ± 0.002 (V10), 0.013 ± 0.002 (V15), 0.012 ± 0.002 (V20) and 0.011 ± 0.002 (V30), leading to quite similar internal and applied fields.

Room temperature magnetic hysteresis loops were measured in a vibrating sample magnetometer (VSM) Lakeshore 7300, with a maximum field up to 1.5 T. The magnetic polarization – as a function of field and temperature – was measured in a MPMS Quantum Design SQUID magnetometer at temperatures ranging from 5 K to 300 K.

Additionally, electrical transport between room temperature and 5 K was measured with the conventional four-probe geometry in a PPMS Quantum Design facility. The external magnetic field was applied perpendicular to the ribbon plane, in a transverse configuration relative to the in-plane current.

The hysteresis loops were analyzed considering a superparamagnetic-like contribution and a mean effective internal field given by [11]:

$$J_{SPM} = J_{S,SPM}\left\{\coth\left(\frac{\mu(H_i + H_i^*)}{k_B T}\right) - \frac{k_B T}{\mu(H_i + H_i^*)}\right\} \quad (1)$$

superimposed, when necessary, to a ferromagnetic one given by [23]:

$$J_{FM} = \frac{2J_{S,FM}}{\pi}\arctan\left[\frac{(H_i \pm H_{iC})}{H_{iC}}\tan\left(\frac{\pi J_{R,FM}}{2J_{S,FM}}\right)\right]. \quad (2)$$

Here, $J_{S,FM}$, $\mu_0 H_{iC}$ and $J_{R,FM}$ are the saturation polarization, the coercive field and the remanent polarization, respectively, associated with the ferromagnetic contribution. $J_{S,SPM}$, μ and $\mu_0 H_i^*$ are respectively, the effective saturation polarization, the mean magnetic moment of the activated particles and a correction to the internal field, introduced in order to consider inter-particle interactions.

3. Results and Discussion

3.1. Microstructures

Fig. 1 displays cross sections of ribbons, showing the grain structure resulting from the special heat extraction conditions in the twin-roller device, at two different wheel speeds. The ribbon thickness may be directly estimated and the different grain structures compared. It may be observed that columnar grains predominate in samples cooled at lower rates, while at higher wheel speeds equiaxed grains develop.

The values for the mean ribbon width (w) and thickness (t), corresponding to each cast condition, are w = 1.45 ± 0.05 mm, t = 78 ± 4 μm (V10); w = 1.75 ± 0.05 mm, t = 65 ± 5 μm (V15); w = 1.30 ± 0.07 mm, t = 55 ± 9 μm (V20) and w = 1.65 ± 0.05 μm, t = 40 ± 3 μm (V30).

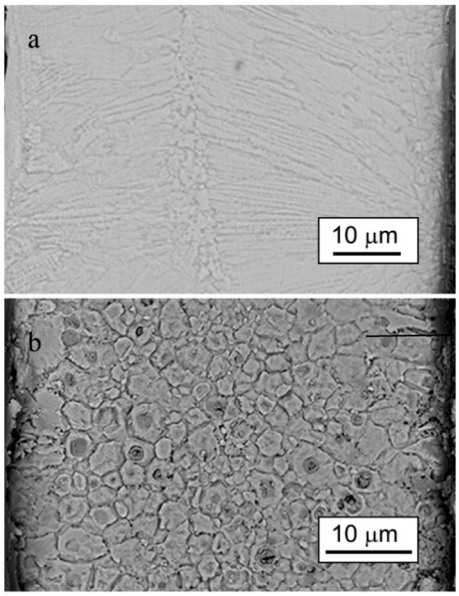

Fig. 1. SEM micrographs of the transversal surface of ribbons V10, $t = 77$ μm (a) and V20, $t = 52$ μm (b), showing the grain structure resulting from the special heat extraction geometry in the twin-roller device.

Although occasional perturbations in the fluid flow may induce alterations in the main pattern, grains are basically columnar or equiaxed. The solidification microstructure observed in samples cooled at low wheel speed (V15 and V10) - illustrated in Fig. 1.a - consists of thin columnar grains, developing from the contact surface to almost the central part of the ribbon, where a relatively thin zone of equiaxed grains (3 μm diameter) is found. Under the rapid solidification conditions imposed in the reported experiments there is not much segregation, and the difference between the structures obtained is related to the evolution of Co within a Cu matrix. The wheel contacted surface region is very small as compared to the microstructure in the inner volume so flakes' characterization by TEM described below is based on this internal zone. Co and Cu are basically immiscible so, decreasing the wheels velocity also decreases the cooling rate, enlarging the time for Co diffusion in the solid state.

XRD results for ribbons obtained with different cooling rates are depicted in Fig. 2. Complete diffractograms corresponding to samples V10 to V30 are shown in Fig. 2.a while a more detailed view of the 35°–60° angular range is provided in Fig. 2.b.

A majority *fcc* Cu(Co) phase is indexed according to the *fcc* Cu (PDF # 00–004-0836; $a = 3.6150$ Å) pattern. A secondary Co-rich phase (P) was also detected as well as a third minority oxide phase, identified as *fcc* CoO (PDF # 00-048-1719; $a = 4.2612$ Å) (indicated by arrows).

Peaks labeled with a question mark "?" could not be indexed. No evidence of spinodal decomposition could be detected. The lattice constants corresponding to the identified phases in all the samples are listed in Table 1. These lattice parameter values are consistent with a mean ribbon density of 8.83 ± 0.01 g/cm^3 which is only 1.2% lower than that given by the rule of mixtures.

Then, microstructure details were investigated by TEM, in particular precipitates (size distribution and localization in the matrix). Grains of about 1 and 5 μm were found, corresponding to the Cu(Co) solid solution *fcc* phase (Fig. 3.a), in agreement with XRD results. Along with dislocations, high-density regions of Co-rich *fcc* precipitates and a quite smaller quantity of larger CoO precipitates are observed within the grains (Fig. 3.b). A closer examination of these Co-rich precipitates confirms that they are coherent with the Cu(Co) matrix, as they exhibit the characteristic butterfly diffraction contrast when observed under two-beam condition, due to lattice mismatch with the matrix [24].

Fig. 4.a shows the typical precipitation substructure corresponding to samples V30. Small coherent precipitates are recognized by their ring-shape strain contrast under bright field zone axis (BFZA) condition [25]. The corresponding precipitate size distribution, obtained from measuring the ring diameters, is presented in Fig. 4.b. The histogram was fitted using a log-normal distribution:

$$f(D) = \frac{1}{\sqrt{2\pi\sigma_P^2} D_P} \exp\left(-\frac{ln^2\left(\frac{D}{D_P}\right)}{2\sigma_P^2} \right) \quad (3)$$

from which parameters D_P (median of the distribution) and σ_P were obtained. These magnitudes and the mean coherent precipitate diameter d_{TEM} and its corresponding standard deviation *sd* are related by the equations:

$$d_{TEM} = D_P \exp(\sigma_P^2/2) \quad (4)$$

$$\sigma_P = \left[\ln\left(1 + \left(\frac{sd}{d_{TEM}}\right)^2\right)\right]^{1/2} \quad (5)$$

A new feature becomes evident in ribbons cooled at lower rates, in which precipitate distributions are non-uniform. Fig. 5 depicts results obtained in samples V20. Regions with a high density of slightly larger Co-rich precipitates are observed in extended zones in the matrix (Fig. 5.a and b) as well as precipitate-free regions (Fig. 5.c). This is illustrated in Fig. 6 for samples V15 and V10. Some grain boundaries are deeply etched by the polishing agent, probably due to the thin pure

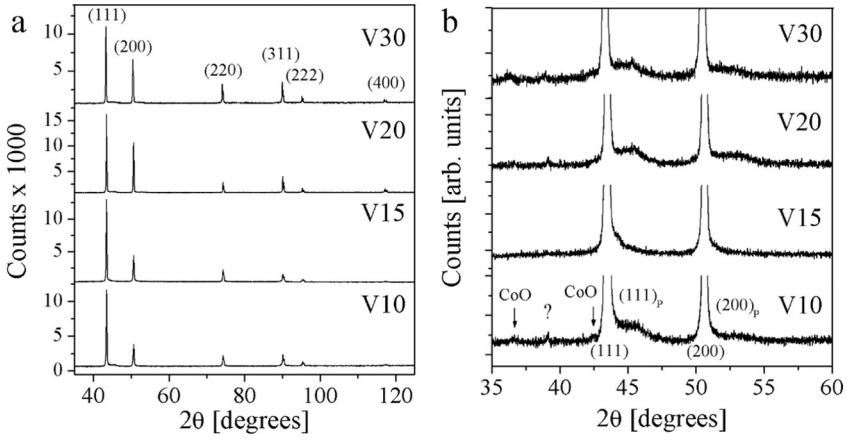

Fig. 2. (a) X-ray diffraction patters corresponding to ribbons processed at different tangential wheel speeds; (b) details of diffractograms in (a) in the range 35° to 60°.

Table 1
Room temperature lattice constants corresponding to the cubic phases detected in ribbons cooled at different rates, after the XRD patterns shown in Fig. 2. *a*: Cu(Co) *fcc* phase, a_P: Co-rich phase, a_{CoO}: *fcc* CoO phase.

Sample	V10	V15	V20	V30
a [Å]	3.6107 ± 0.0005	3.6112 ± 0.0005	3.6128 ± 0.0005	3.6110 ± 0.0005
a_P [Å]	3.505 ± 0.005	3.564 ± 0.005	3.503 ± 0.005	3.496 ± 0.005
a_{CoO} [Å]	4.265 ± 0.005	4.261 ± 0.005	4.267 ± 0.005	4.264 ± 0.005

Cu film frequently found in boundaries, associated with the positive segregation enthalpy of Co in Cu [3,26]. Inside the grains and near boundaries, high-density colonies of coherent Co-rich precipitates are identified. These colonies are prone to appear in the matrix zones where Co atoms segregate during very early stages of the cooling process. In fact, Small Angle Neutron Scattering measurements on dilute Cu-Co alloys [2] confirm the existence of extended compositional fluctuations, which precede the formation of *fcc* Co-rich precipitates. Colonies observed in samples in Fig. 6 are certainly related to these compositional fluctuations. Smaller coherent precipitates may develop between colonies, leading to a bimodal size distribution as it is clearly defined in the image and histogram of sample V15, shown in Fig. 7. In addition, large CoO incoherent precipitates also grow inside the colonies and/or in regions in-between. Fig. 8 shows the precipitation substructure in a typical sample V10 colony and the coherent Co-rich precipitates size distribution is shown in Fig. 8.b together with the log-normal best fit to the profile.

Regarding the composition of these coherent Co-rich precipitates, A. Hutten and G. Thomas [27] reported values of 98 ± 2 at.% Co and 2 ± 2 at.% Cu for a $Cu_{65}Co_{35}$ alloy. These values support the assumption of a precipitate saturation polarization of $J_{S,Co} = 1.82$ T, equal to that corresponding to pure Co.

The actual precipitates mean sizes d_P are listed in Table 2. Considering a constant $K_1 = 6.2 \times 10^4$ J/m^3 at room temperature for the *fcc* Co magnetic anisotropy [28], the limit superparamagnetic size becomes $d_{SPM} = (25k_BT/K_1)^{1/3} \cong 12$ nm. This critic size is indicated by a dotted

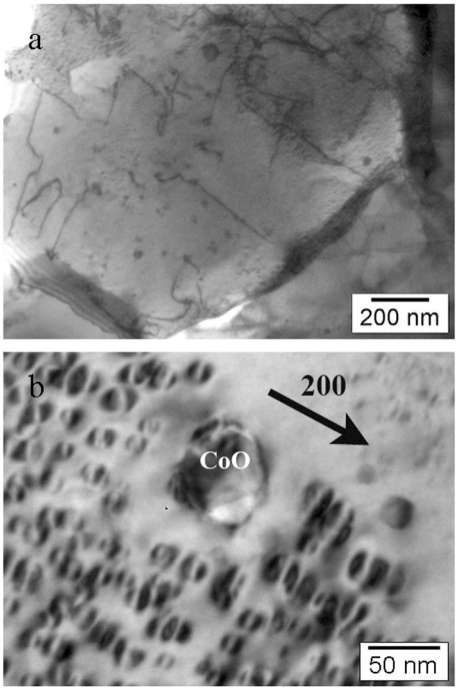

Fig. 3. Bright field (BF) TEM image under two beam condition with g = 200, showing (a) dislocations in a Cu(Co) *fcc* matrix grain and (b) coherent precipitates with butterfly diffraction contrast and a bigger CoO precipitate. These images correspond to sample V15 but represent the general microsctructure of all the samples.

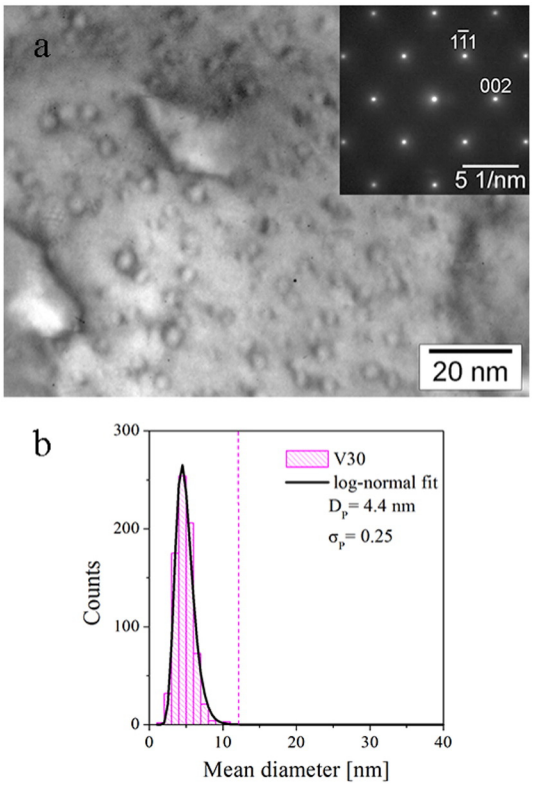

Fig. 4. (a) Ring-shape coherent Co-rich precipitates under bright field imaging from [110] zone axis in sample V30. (b) Precipitate size histogram; full line corresponds to the better fit of a log-normal distribution. Dotted vertical line indicates the paramagnetic size limit at room temperature.

vertical line in the histograms corresponding to the different samples. It may be then concluded that in samples V30 and V20 Co precipitates are unblocked at 300 K, whereas in samples V15 and V10 a considerable amount is blocked at room temperature and undergo a ferromagnetic behavior. The precipitate density was roughly estimated by choosing regions in the sample with constant thickness (well defined contours contrast), working in zone axis orientations. Assuming a thickness near 75 nm, the mean values resulting from ten determinations on each sample were 5×10^{16} cm^{-3} (colonies V10), 8×10^{16} cm^{-3} (colonies V15), 18×10^{16} cm^{-3} (V20) and 22×10^{16} cm^{-3} (V30). It is worth noting that Co precipitates exhibit a clearly bimodal size distribution in samples V15 (Fig. 7) and a quite wide one in V10 (Fig. 8). Only one precipitate family, smaller in size and with a narrow distribution, was detected in samples cooled at higher rates. The volume fraction of low density and/or precipitate free zones increases with the wheel speed. These zones are undetectable in samples V30 but they reach a volume fraction near 0.7 in samples V10, illustrating the increasing packing of larger Co precipitates in the matrix.

Finally, results of electron diffraction are consistent with those of XRD in connection with coherent Co and incoherent CoO precipitates. To find additional reflections corresponding to the coherent precipitates, higher order reflections were excited, as illustrated in Fig. 9.a. A long exposure image of reflection 600 and 800 reveals an additional spot corresponding to the coherent precipitates (Fig. 9.b). The ratio between inter-planar distances of coherent precipitates and the matrix were calculated from these electron diffraction patterns, obtaining: $a_p/a_{matrix} \sim 0.98$ (TEM) ($a_p/a_{matrix} \sim 0.97$ (XRD)). Similar conclusions were drawn when comparing these ratios for the CoO precipitates and the Cu(Co) matrix: $a_{CoO}/a_{matrix} \sim 1.17$ (TEM) ($a_{CoO}/a_{matrix} \sim 1.18$ (XRD)). Moreover, the latter quotients are indistinguishable from $a_{CoO}/a_{Cu} = 1.179$, obtained by using the lattice parameters tabulated values for the CoO and Cu phases (PDF # 00–048-1719 and 00–004-0836, respectively).

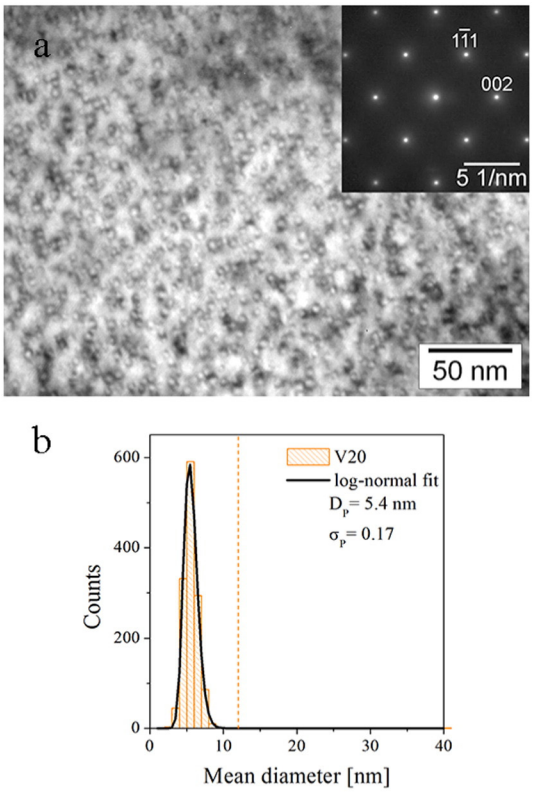

Fig. 5. (a) TEM image of sample V20 showing coherent Co-rich precipitates with ring contrast under BFZA [110] condition. (b) Precipitate size histogram; the full line corresponds to the better fit of a lognormal distribution. The distribution median size value and the respective deviation are indicated. (c) Precipitate-free region and dislocations in sample V20.

Although all samples were carefully inspected, no evidence of the laminar-like segregation - observed by other authors in quenched and further annealed Cu-Co ribbons - could be detected neither by TEM nor by XRD [4,14]. Hence, it may be concluded that in these twin-roller melt-spun ribbons, in the as-cast state, only Co precipitates are present, with size and spatial distributions quite similar to those observed in alloys with good MR properties [7,8].

Summarizing, the effects of cooling rate on the main microstructure features observed in twin-rolled $Cu_{90}C_{10}$ ribbons are:

- Coherent Co-rich precipitates are larger in samples cooled at lower rates (~4 nm in V30 to ~13 nm in V10).
- Size distributions are narrow in samples cooled at 20 m/s and 30 m/s but they are quite wide (even bimodal) in samples cooled at 10 m/s and 15 m/s. In these latter samples a significant portion of particles are blocked and behave as ferromagnetic units.

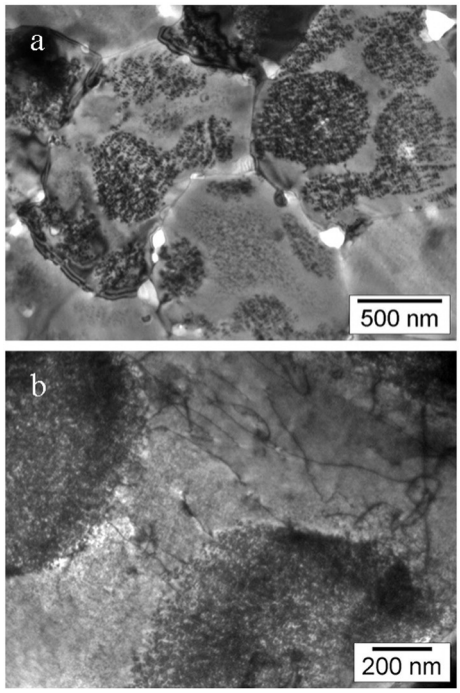

Fig. 6. TEM Bright field images of (a) sample V15 and (b) sample V10. Non-uniform distribution of coherent precipitates, forming colonies, can be observed.

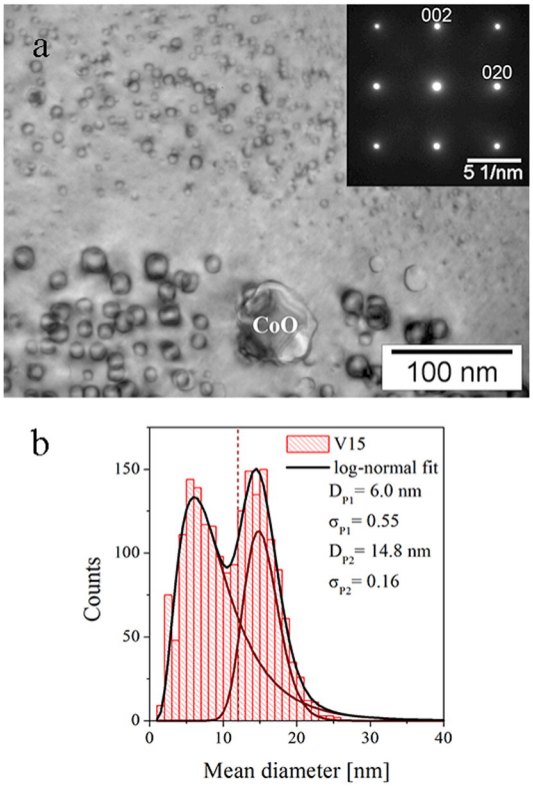

Fig. 7. Ring-contrast coherent Co precipitates in sample V15 under bright field imaging from [100] zone axis. A heterogenic spatial distribution is observed: (b) bimodal distribution of coherent precipitates together with a larger CoO particle (60 nm). (c) Precipitate size histograms and their log-normal fittings. The median size values and the respective deviations of the bimodal distribution are indicated.

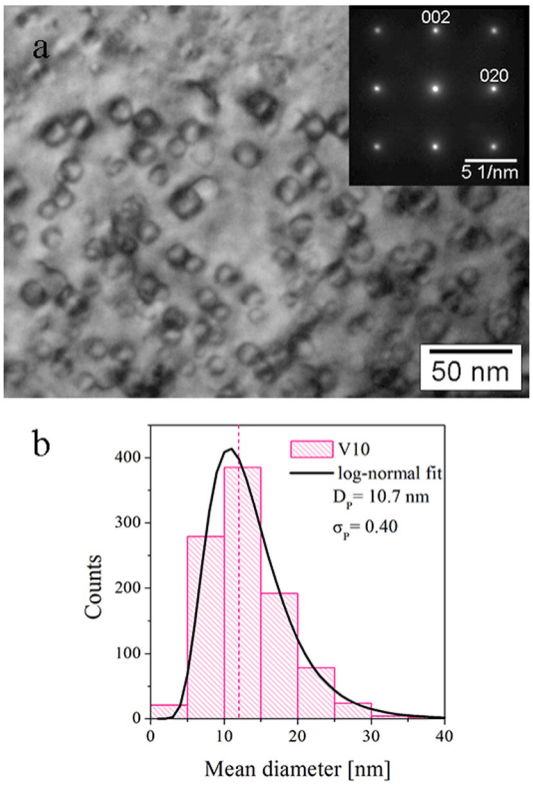

Fig. 8. (a) TEM image of sample V10 showing coherent Co-rich precipitates with ring contrast, corresponding to a BFZA [100]. (b) Histogram of precipitate size; the full line corresponds to the better fit of a log-normal distribution. The median size value D_P and the corresponding deviation σ_P are indicated.

- As the wheel speed decreases the precipitate spatial distribution becomes non-uniform; it changes from a dense and homogeneous distribution in V30 (2×10^{17} cm^{-3}) to larger precipitates condensed in colonies, with somewhat lower density ($0{,}8 \times 10^{17}$ cm^{-3}) in V10 and V15 samples. In the inter-colony space smaller particles or even precipitate free zones are found.
- Samples V20 (5 nm) exhibit larger precipitates than V30 (4 nm), and quite similar volume densities. In addition, the spatial precipitate distribution in V20 is less uniform than in V30. These two features are likely to promote strong inter-particle interactions.
- A small volume fraction of CoO is detected in the samples by the quite small peaks in the XRD difractograms and TEM observations. Cobalt oxide is antiferromagnetic, with a Neel temperature T_N ~ 290 K, but neither a sharp drop above this temperature is observed in FC curves, nor any exchange bias effect in the hysteresis loops, further supporting the conclusion of a small oxide volume fraction.

Table 2
Microstructure and magnetic parameters corresponding to the samples investigated. The mean Co precipitate diameter obtained by TEM, d_{TEM} and from the hysteresis loop d_{loop}, are listed together with the superparamagnetic saturation polarization $J_{S,SPM}$, the mean interaction field $\mu_0 H^*$, the observed remanence $J_{R,SPM}$ and the effective magnetic moment μ, corresponding to the superparamagnetic contribution to the hysteresis loops in Fig. 10. The maximum reduced remanence m_R^{max} associated to this superparamagnetic contribution and the interaction field parameter $\mu_0 \dot{H}_0$, defined in Eq. (6) [11] are also quoted.

Sample	V10	V15	V20	V30
d_{TEM} [nm]	12 ± 5	7 ± 3 15 ± 2	5 ± 1	4 ± 1
d_{loop}[nm]	10 ± 1	7 ± 1	6 ± 1	4 ± 1
$\mu_0 H^*$ [mT]	20 ± 3	16 ± 2	34 ± 2	2 ± 1
$J_{S,SPM}$ [mT]	11 ± 1	15 ± 2	70 ± 1	30 ± 1
μ [10^{-20} J/T]	85 ± 5	28 ± 3	15 ± 1	6 ± 1
$J_{R,SPM}$ [mT]	10 ± 1	4 ± 1	32 ± 1	0.2 ± 1
m_R^{max}	0.89	0.249	0.453	0.007
$\mu_0 \dot{H}_0$ [mT]	13 ± 1	8 ± 1	38 ± 1	2 ± 1

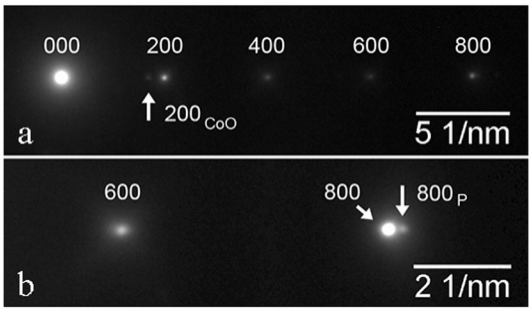

Fig. 9. SAED pattern of a 200 systematic row in sample V15. a) Low exposure image showing the 200 CoO extra reflection. b) Large exposure image of the faint reflections in a) showing the 800 reflection, corresponding to the coherent precipitates.

These microstructures are ideal systems to apply existing models, describing the magnetic polarization vs. applied field curves of ensembles of small, *interacting superparamagnetic* particles [11,12,21]. Also, the effect of size distribution on the hysteresis properties [10], and/or the magnitude of the *granular* contribution to the observed GMR in these alloys may be estimated [7].

3.2. Magnetic Properties

The room-temperature magnetic hysteresis loops corresponding to samples cooled at different wheel speeds are plotted in Fig. 10. Sample V30 displays superparamagnetism whereas the other loops exhibit a small coercivity which has been ascribed to either superparamagnetism with interactions, or to ferromagnetic Co-rich strips developed by spinodal decomposition or by discontinuous precipitation of a laminar phase. It has been previously concluded that these latter contributions may be disregarded. Therefore, to explain the deviation of the $J(H)$ curve from the Langevin curve, only inter-particle interactions and/or large blocked particles should be considered.

Table 3 indicates room-temperature coercive field values (defined as the internal field at which total polarization vanishes $\mu_0 H_i$ ($J = 0$)), total remanent and saturation polarization corresponding to loops in Fig. 10.

Samples V30 and V20 loops are well fitted by considering a Langevin function with a modified argument $(\frac{\mu \mu_0 H_{eff}}{k_B T})$, where $\mu_0 H_{eff} = \mu_0 H_{app} \pm \mu_0 H^*$ is given by the superposition of the applied field and a constant mean field $\mu_0 H^*$, arising from dipolar interactions between non-

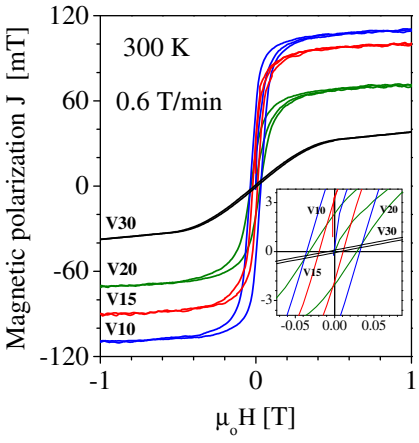

Fig. 10. Magnetic polarization vs. the applied magnetic field, at room temperature, corresponding to samples solidified at different cooling rates.

Table 3
Hysteresis parameters corresponding to the major loops in Fig. 10. The internal coercive field for $J = 0$, $\mu_0\, {}_JH_{iC}$, remanent polarization J_R and saturation polarization J_S.

Sample	V10	V15	V20	V30
$\mu_0\, {}_JH_{iC}$ [mT]	34 ± 4	20 ± 4	31 ± 4	7 ± 4
J_R [mT]	54 ± 2	32 ± 2	23 ± 2	1 ± 2
J_S [mT]	109 ± 3	100 ± 3	72 ± 3	40 ± 3

monodisperse particles. On the other hand, samples V15 and V10 are described considering superparamagnetic-like and ferromagnetic components, the latter regarding the contribution from large blocked particles (≥12 nm) in the distribution. The distribution parameters corresponding to the superparamagnetic-like contribution to the major loop are listed in Table 2.

3.2.1. Mean Field Models

Rigorously, superparamagnetism involves unblocked, non-interacting particles with a unique magnetic moment. As herein coherent precipitates are pure Co, the conditions for a uniform magnetic moment and uniform volume are equivalent.

In the analyzed samples, neither the non-interactions hypothesis nor the monodisperse particles one are completely fulfilled. V30 samples are the closest to satisfy these two conditions. Although size distribution remains quite narrow in V20, colonies with a high density of larger precipitates are observed, which undergo stronger dipolar interactions responsible for the coercivity detected. V15 and V10 size distributions are quite wide so, interacting superparamagnetic and ferromagnetic contributions to the hysteresis loop are expected.

Allia et al. [11] explain the magnetic hysteresis in these granular systems in terms of dipolar interactions between magnetic-metal particles (coherent Co precipitates in this case), which hinder the system response to the applied field. These authors describe these interactions in a mean-field scheme, by introducing a memory term in the argument of the Langevin function, describing the anhysteretic behavior of assembled ideal non-interacting and monodisperse superparamagnetic particles. The *rms* field arising from the cumulative effect of dipolar interactions $(\mu_0\hat{H}_0)$ is linked in the theory to a measurable quantity: the reduced remanence of a major symmetric hysteresis loop. Following [11], this field satisfies the relationship:

$$\frac{J_{R,SPM}}{J_{S,SPM}} = m_R^{max} = L\left(\frac{\mu\,\hat{H}_0}{k_BT}\right) \cong \frac{1}{3}\frac{\mu\,\hat{H}_0}{k_BT} \tag{6}$$

where $J_{R,SPM}$ and $J_{S,SPM}$ are, respectively, the remanent and the saturation polarization of the superparamagnetic-like contribution to the major loop, μ is the mean value of the superparamagnetic individual moment, k_B is the Boltzmann constant and T the absolute temperature. The magnitude of $m_R^{max}$is the maximum of the plot $\Delta_R\,(m)$ with

$$\Delta_R(H) = \frac{1}{2}\frac{J^+(H) - J^-(H)}{J_{S,SPM}} \tag{7}$$

and

$$m(H) = \frac{1}{2}\frac{J^+(H) + J^-(H)}{J_{S,SPM}} \tag{8}$$

Here, $J^{\pm}$ is the upper/lower polarization branch of the superparamagnetic-like loop and $J_{S,SPM}$,the superparamagnetic saturation polarization. The relative half-sum $(m(H))$, has been proven to exactly coincide with the anhysteretic relative magnetization curve [11]. This anhysteretic curve provides a quite accurate approximation to the magnetization behavior of the granular system, in which the interaction among particles has been turned off. The curves $\Delta_R\,(m)$ vs. m are displayed in Fig. 11. As expected for magnetic dipolar interaction effects,

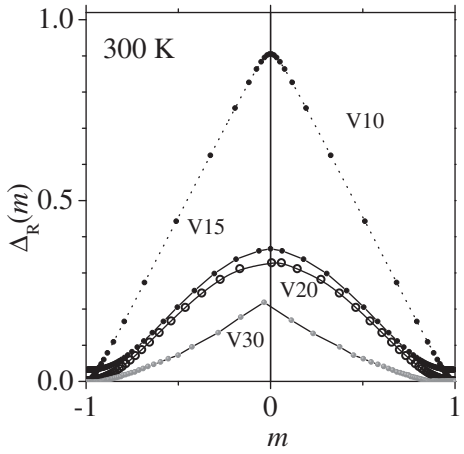

Fig. 11. Δ_R vs. m curves corresponding to the samples investigated. The maximum m_R^{max} indicates the relative remanence corresponding to the superparamagnetic-like contribution to the hysteresis loops displayed in Fig. 10.

the relative remanence increases with the mean unblocked precipitate size. Measured values of m_R^{max} from Fig. 11 are listed in Table 2, along with the resulting values of the maximum interaction field $\mu_0\hat{H}_0$, estimated using Eq. (6).

Another feature which leads to deviations from the ideal superparamagnetic behavior is the non-homogeneous spatial distribution of magnetic moments. Sánchez et al. [21] have recently described the effect of a non-uniform spatial distribution of precipitates on the anhysteretic curve by a mean demagnetizing field $\mu_0 H_{mean} = -N_{eff}J$, considering interactions on the magnetic response of the precipitate arrays. This effective demagnetization factor depends on the specimen demagnetizing factor, the cluster (colony) shape, and on the mean distance between near-neighbor nanoparticles and among colonies. The effective demagnetizing factor of the sample is given by:

$$N_{eff} = \frac{\gamma_{C-1}^3}{\varphi_C}N_C + N_z \tag{9}$$

where $\gamma_C = \frac{\lambda_C}{d_C}$; being d_C and λ_C the mean diameter of these colonies and the distance between them, and $\varphi_C = n_C\gamma_C^3 d_C^3$ with n_c the number of colonies per unit volume. $N_C \cong 1/3$ and N_z are the demagnetizing factors of a spherical colony (see Fig. 6) and of a ribbon, respectively. Assuming values of $\gamma_C \approx 1.6$ and $\varphi_C \approx 0.7$, the contribution of the first term in Eq. (9) to N_{eff} becomes $0.72 \gg 0.017$ indicating that, in our samples, magnetostatic effects arising from the sample shape (ribbon) are negligible when compared to those related to colony shape and/or precipitate density inside them. This model describes the anhysteretic behavior rather than the low coercivity observed in superparamagnetic-like samples.

3.3. Magnetoresistance

Shufeng Zhang and Peter M. Levy [9] have described the conductivity in granular systems based on similar considerations to those applied in multilayered structures in CPP geometry. Magnetoresistance MR (frequently defined as MR (J, T, *microstruc.*) = (J(H) - J(H = 0))/J(H = 0)) is proposed to mainly originate from the spin-dependent scattering at the interfaces between granules and the matrix, and to a much lesser extent, from the spin-dependent scattering within granules. The size distribution of these granules is of great importance to explain experimental MR results [10] as it is equivalent to the layer thicknesses in multilayered structures. The remaining five parameters in the model are the mean-free path in the matrix λ_m, inside the granules (precipitates) λ_P and at the interfaces λ_S, and the ratios of the

spin-dependent to spin-independent potentials for the granules (p_b) and for the interfaces (p_s).

MR curves corresponding to the twin-rolled samples are depicted in Fig. 12, which confirms that absolute MR values become larger as the mean precipitate size decreases. At 300 K, MR decreases almost linearly up to the maximum field applied, whereas at 5 K, V30 and V20 curves tend to saturate, behaviors which have already been reported for this alloyed system.

Ferrari et al. [10] have demonstrated that in monodisperse precipitate systems, in which interactions may be neglected, both ΔR and $\Delta R/R$ are proportional to the square of the total relative superparamagnetic magnetization $(J_{SPM}/J_{S,SPM})^2 = m(H)^2$. In addition, they found that when $p_s > p_b$, as in Co/Cu, both magnitudes increase as the granule size decreases. For these ideal superparamagnetic systems, the plot of the normalized magnetoresistance $MR_n(=MR/MR_{sat})$ as a function of the anhysteretic relative polarization $m(H)$ given by Eq. (8), is a parabola (Fig. 13). Similar plots corresponding to the measured samples are included in this figure. MR_n vs. M/M curve in sample V30, is close to the parabolic behavior near saturation, but it flattens in the low-magnetic field region. On the other hand, curves corresponding to V10, V15 and V20, exhibit little compliance with the square law of the magnetoresistance as a function of magnetization.

Such a large deviation from the quadratic behavior at low fields is frequently observed and it cannot be entirely attributed to a distribution of magnetic moments. Therefore, a contribution from interparticle interactions should be considered. The existence of correlations between magnetic moments (precipitates) and the presence of strong magnetic interactions is confirmed by different experimental techniques [13]. The magnitude of interactions not only depends on the spatial distribution of precipitates (shorter inter-precipitate distances strengthen magnetic interactions) but also on the presence of large blocked particles. Correlations between superparamagnetic and blocked particles are known to affect the magnetization behavior [29]. In fact, the small hysteresis often displayed by the polarization curves of granular systems may be attributed to blocked particles, even at room temperature, or to strong interactions between the magnetic precipitates. These phenomena are likely to explain the large experimental deviations from the parabolic behavior of the magnetoresistance vs magnetization curves, observed in Fig. 13.

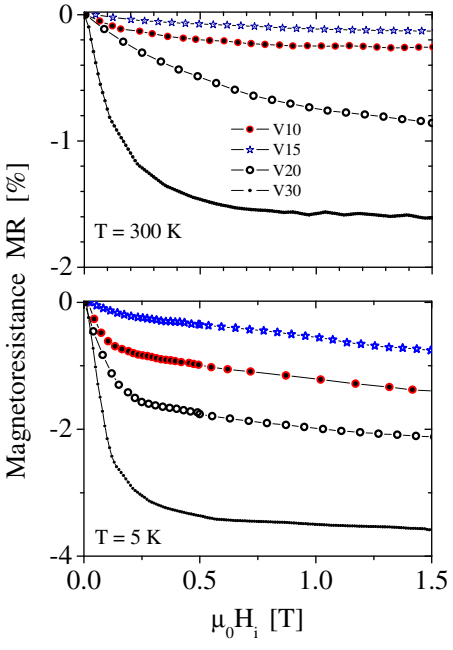

Fig. 12. Magnetoresistance vs. the applied magnetic field, at two temperatures, measured in samples solidified at different cooling rates.

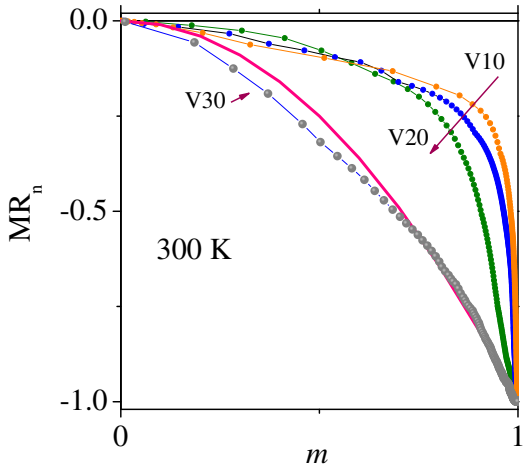

Fig. 13. Normalized magnetoresistance vs. the anhysteretic polarization, at room temperature, corresponding to samples solidified at different cooling rates.

4. Conclusions

The microstructures obtained by twin-roller melt-spinning at different wheel speeds are for the first time characterized, and their respective hysteresis and charge/spin properties, evaluated.

This processing method provides scenarios in which a different phase selection takes place. The microstructures are quite different from those resulting from *rapid solidification-thermal annealing* routes, since no multilayer-like phases (spinodal-like or discontinuous precipitation type) are detected. Instead, coherent *fcc* Co precipitates are directly found in the as-cast condition, whose size is comparable to those observed in high-temperature annealed or Joule-heated samples.

In samples cooled at the highest rate, these precipitates look uniformly distributed inside the grains. However, at lower rates they are grouped in colonies, which are associated with compositional fluctuations reported to appear at high temperatures. Smaller coherent precipitates may form between these colonies, leading in some cases (V15) to a bimodal size distribution. Large, incoherent Co-rich precipitates also form inside the colonies and/or in regions in-between.

In samples V30, a high density of small coherent Co precipitates - uniformly distributed in the matrix - promotes a quasi-superparamagnetic behavior, with little evidence of inter-particle interactions. Accordingly, these samples show the best magnetoresistance ratios at all temperatures.

Ribbons solidified at lower wheel speeds undergo an interacting superparamagnetic behavior promoted by larger precipitates, grouped in high density zones or colonies. Dipolar interaction becomes more important in ensembles of larger particles (magnetic moments) in closer configurations, and/or in samples with a large proportion of blocked particles, such as V15 and V10.

It has been observed that interactions among relatively small precipitates in close packed configurations provide the main contribution to the hysteresis properties observed in these samples, as evidenced by the mean interaction fields corresponding to V20.

In sample V15 most precipitates forming colonies are blocked, whereas the smaller ones are located between colonies. The low values obtained from the effective interaction fields between blocked and unblocked particles indicate that they have relatively little effect in hindering the ideal superparamagnetic response of smaller precipitates. Finally, room temperature MR values associated with granular scattering units are far from the 5–6% measured when spinodal composition profiles are also detected. Therefore, the large MR measured in samples annealed after rapid solidification may be attributed to the spinodally segregated matrix.

Acknowledgements

The authors wish to thank SECyT-UNC -Argentine, Program 2014-2015, Cod. P 05/BP13, MINCyT-Cordoba, Project No 000113/2011 and CONICET Proj. PIP11220090100951, Argentina for the financial support given to this work.

References

[1] T. Nishizawa, K. Ishida, The Co–Cu (cobalt-copper) system, Bull. Alloy Phase Diagr. 5 (2) (1984) 161–165.
[2] W. Wagner, The influence of precursor fluctuations on the kinetics of Co precipitation in dilute CuCo alloys, Acta Metall. Mater. 38 (12) (1990) 2711–2719.
[3] A. Bachmaier, M. Pfaff, M. Stolpe, H. Aboulfad, C. Motz, Phase separation of a supersaturated nanocrystalline Cu–Co alloy and its influence on thermal stability, ActaMaterialia 96 (2015) 269–283.
[4] N.M. Suguihiro, Y.T. Xing, D. Haeussler, W. Jaeger, D.J. Smith, E. Baggio-Saitovitch, I.G. Solorzano, J. Mater. Sci. 49 (18) (2014) 6167–6179.
[5] B. Idzikowski, U.K. Rößler, D. Eckert, K. Nenkov, K.-H. Müller, Spin-glass–like ordering in giant magnetoresistiveCuCo, Europhys. Lett. 45 (6) (1999) 714–720.
[6] L.M. Fabietti, J. Ferreyra, M. Villafuerte, S.E. Urreta, S.P. Heluani, Kondo-like effect in magnetoresistiveCuCo alloys, Phys. Rev. B 82 (2010), 172410.
[7] A.E. Berkowitz, J.R. Mitchell, M.J. Carey, A.P. Young, S. Zhang, F.E. Spada, F.T. Parker, A. Hutten, G. Thomas, Giant magnetoresistance in heterogeneous Cu-Co alloys, Phys. Rev. Lett. 68 (25) (1992) 3745–3748.
[8] P. Allia, M. Knobel, P. Tiberto, F. Vinai, Magnetic properties and giant magnetoresistance of melt spun granular $Cu_{100-x}Co_x$ alloys, Phys. Rev. B 52 (21) (1995) 15398–15411.
[9] S. Zhang, P.M. Levy, Conductivity and magnetoresistance in magnetic granular films, J. Appl. Phys. 73 (1993) 5315.
[10] E.F. Ferrari, F.C.S. da Silva, M. Knobel, Theory of giant magnetoresistance in granular alloys, Phys. Rev. B 59 (13) (1999) 8412–8415.
[11] P. Allia, M. Coisson, M. Knobel, P. Tiberto, F. Vinai, Magnetic hysteresis based on dipolar interactions in granular magnetic systems, Phys. Rev. B 60 (17) (1999) 12207–12218.
[12] P. Allia, M. Coisson, P. Tiberto, F. Vinai, M. Knobel, M.A. Novak, W.C. Nuñes, Granular Cu-Co alloys as interacting superparamagnets, Phys. Rev. B 64 (2001) 144420.
[13] A.D.C. Viegas, J. Geshev, L.S. Dorneles, J.E. Schmidt, M. Knobel, Correlation between magnetic interactions and giant magnetoresistance in melt-spun $Co_{10}Cu_{90}$ granular alloys, J. Appl. Phys. 82 (6) (1997) 3047–3053.
[14] M.G.M. Miranda, E. Estevez-Rams, G. Martinez, M.N. Baibich, Phase separation in $Cu_{90}Co_{10}$ high-magnetoresistance materials, Phys. Rev. B 68 (014434) (2003) (014434-1 to 8).
[15] M.G.M. Miranda, A.T. da Rosa, R. Hinrichs, U. Golla-Schindler, A.B. Antunes, G. Martinez, E. Estevez-Rams, M.N. Baibich, Spinodal decomposition and giant magnetoresistance, Physica B 384 (2006) 175-17.
[16] Marines Grande Malcum Miranda Magnetotransport and Structure in CuCo. (Doctoral Thesis), Universidade Federal do Rio Grande do Sul, Porto Alegre Brazil, 2015.
[17] G. Juarez, M. Villafuerte, S. Heluani, L.M. Fabietti, S.E. Urreta, Magnetic, resistive and magnetoresistive properties of melt spun CoCu alloys, J. Magn. Magn. Mater. 320 (2008) e22–e24.
[18] Y. Zhang, Modelling of Vertical Twin-Roll Casting of Magnesium Alloy. (Master of Engineering Thesis), 2012. University of Wollongong, Faculty of Engineering, 2012. http://ro.uow.edu.au/theses/3534.
[19] A. Hadadzadeh, M.A. Wells, I.-H. Jung, Scale-up modeling of the twin roll casting process for AZ31 magnesium alloy, J. Manuf. Process. 16 (4) (2014) 468–478.
[20] C.A. Santos, J.A. Spim Jr., A. Garcia, Modeling of solidification in twin-roll strip casting, J. Mater. Process. Technol. 102 (2000) 33–39.
[21] F.H. Sánchez, P. Mendoza Zélis, M.L. Arciniegas, G.A. Pasquevich and M.B. Fernández van Raap, Dipolar Interaction and Demagnetizing Effects in Magnetic Nanoparticle Dispersions: Introducing the Mean Field Interacting Superparamagnet, Model (MFISP Model), *arXiv.org>cond-mat>arxiv*:1507.05192.
[22] P. Landeros, J. Escrig, D. Altbir, D. Laroze, J. d'Albuquerque, E. Castro, P. Vargas, Scaling relations for magnetic nanoparticles, Phys. Rev. B 71 (2005) 094435.
[23] M. Stearns, Y. Cheng, Determination of para and ferromagnetic components of magnetization and magnetoresistance of granular Co/Ag films, J. Appl. Phys. 75 (1994) 6894.
[24] M.F. Ashby, L.M. Brown, Diffraction contrast from spherically symmetric coherency strains, Philos. Mag. 8 (9) (1963) 1083–1103.
[25] R. Hattenhaner, F. Haider, Improved imaging of small coherent precipitates by bright field/zone axis incidence TEM, Scr. Metall. Mater. 25 (1991) 1173.
[26] J.R. Trelewicz, C.A. Schuh, Grain boundary segregation and thermodynamically stable binary nanocrystalline alloys, Phys. Rev. B 79 (2009) 094112.
[27] A. Hutten, G. Thomas, Investigation of heterogeneous $Cu_{1-x}Co_x$ alloys with giant magnetoresistance, Ultramicroscopy 52 (1993) 581–590.
[28] Alberto P. Guimarães, Principles of Nanomagnetism, 2009, Springer-Verlag Berlin Heidelberg, pag. 78, DOI http://dx.doi.org/10.1007/978-3-642-01482-6
[29] N. Wiser, Phenomenological theory of the giant magnetoresistance of superparamagnetic particles, J. Magn. Magn. Mater. 159 (1–2) (1996) 119–124.